



**HAL**  
open science

# Optimal dual-PZT sizing and network design for baseline-free SHM of complex anisotropic composite structures

Emmanuel Lize, Marc Rébillat, Nazih Mechbal, Christian Bolzmacher

## ► To cite this version:

Emmanuel Lize, Marc Rébillat, Nazih Mechbal, Christian Bolzmacher. Optimal dual-PZT sizing and network design for baseline-free SHM of complex anisotropic composite structures. *Smart Materials and Structures*, 2018, 10.1088/1361-665X/aad534 . hal-01891029v1

**HAL Id: hal-01891029**

**<https://hal.science/hal-01891029v1>**

Submitted on 9 Oct 2018 (v1), last revised 5 Jul 2019 (v2)

**HAL** is a multi-disciplinary open access archive for the deposit and dissemination of scientific research documents, whether they are published or not. The documents may come from teaching and research institutions in France or abroad, or from public or private research centers.

L'archive ouverte pluridisciplinaire **HAL**, est destinée au dépôt et à la diffusion de documents scientifiques de niveau recherche, publiés ou non, émanant des établissements d'enseignement et de recherche français ou étrangers, des laboratoires publics ou privés.

# 1 Optimal dual-PZT sizing and network design for baseline-free 2 SHM of complex anisotropic composite structures

3 Emmanuel LIZÉ<sup>1</sup>, Marc RÉBILLAT<sup>2</sup>, Nazih MECHBAL<sup>2</sup> and Christian BOLZMACHER<sup>1</sup>

4  
5 <sup>1</sup> CEA, LIST, Sensorial and Ambient Interfaces Laboratory, 91191 - Gif-sur-Yvette CEDEX, France.

6 <sup>2</sup> Processes and Engineering in Mechanics and Materials Laboratory (CNRS, CNAM, ENSAM), 151,  
7 Boulevard de l'Hôpital, Paris, F-75013, France.

8  
9 E-mail: [emmanuel.lize@cea.fr](mailto:emmanuel.lize@cea.fr)

10  
11 **Keywords:** Structural Health Monitoring, Lamb Waves, dual PZT, anisotropic composite structure,  
12 mode decomposition, baseline free methods.

## 13 Abstract

14 Structural Health Monitoring (SHM) processes for aeronautic composite structures are generally  
15 based on the comparison between healthy and unknown databases. The need for prior baseline signals  
16 is one of the barriers to an industrial deployment and can be avoided with “*baseline-free*” SHM (BF-  
17 SHM) methods based on the attenuations and reflections of symmetric and antisymmetric Lamb waves  
18 modes attributable to a damage. A promising mode decomposition method is based on the use of dual  
19 PZTs (concentric disc and ring electrodes lying on a single PZT). However, performances of such  
20 methods highly depend on the Lamb wave modes properties (propagation speed and attenuation that  
21 vary with material orientation and inter-PZT distance), the number and the sensitivity of the dual PZT  
22 to each mode (which depends on the frequency and element size). Considering these constraints, an  
23 original three-step process able to design a full dual-PZT network and the optimal range of excitation  
24 frequencies to consider on a highly anisotropic and arbitrarily complex aeronautic structure is presented.  
25 First, the dispersion curves of Lamb waves in the investigated material together with the minimal size

26 of the damage to detect are used to estimate the size of the dual PZT as well as convenient excitation  
27 frequencies. A Local Finite Element Model representative of the full-scale structure is then used to  
28 estimate optimal distance and orientation between neighbor PZTs elements. Finally, a network  
29 optimization solver applies these parameters to place dual-PZTs on a fan cowl of an aircraft nacelle and  
30 provides a candidate network covering the whole structure.

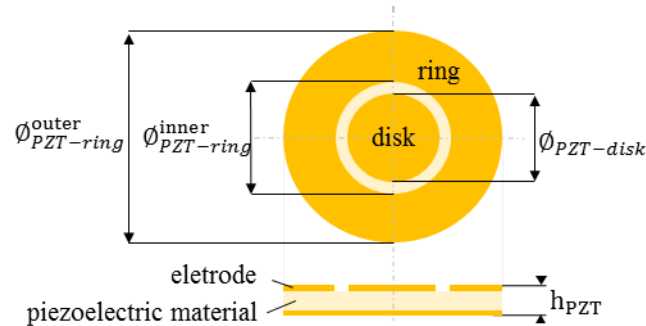
## 31 1. Introduction

32 Monitoring in real-time and autonomously the health state of structures is referred to as Structural  
33 Health Monitoring (SHM) [1]. Damage detection using Lamb waves is one of the most common method  
34 for the SHM of aeronautic composite structures. Among all the methods employed to trigger and catch  
35 Lamb waves, the use of piezoelectric transducer (PZT) is one of the cheapest and easiest-to-settle. The  
36 common approach is based on the comparison of signals recorded on a “pristine” structure - the baseline  
37 - against those obtained on a possibly damaged structure. The resulting signals that will be used to  
38 elaborate damage indexes strongly depend on the structure’s mechanical and geometrical properties as  
39 well as on environmental conditions. Some solutions have been proposed to compensate for the effect  
40 of temperature [2-5] or to extend baseline data to a wider range of environmental conditions [6, 7]. This  
41 drawback of existing methods has also fed the interest for “baseline-free” methods. “Baseline-free” is  
42 here an abusive word (see Axiom II in [1]) since data, models, or physical assumptions are always  
43 needed to decide whether a structure is damaged or not. This expression thus refers here to methods  
44 where prior reference signals recorded from the pristine condition of the monitored structure is not  
45 necessary for damage detection.

46 Symmetric and antisymmetric Lamb wave modes are very useful for SHM as they convey  
47 complementary information when interacting with damages [8], [9, Ch. 19.4]. Lamb wave modes are  
48 related to Lamb solutions for wave propagations in isotropic plates but are also commonly (and  
49 abusively) used to designate plate-like waves that propagate in anisotropic materials. Early studies on  
50 damage detection in composite structures stated that  $S_0$  mode was more appropriate than  $A_0$  mode for  
51 delamination detection since it exhibits higher sensitivity in the structural thickness [8, Para. 3.3]. In

52 most SHM application on composite structures,  $S_0$  mode is actually preferred since it has lower  
53 attenuation, allowing for larger distances between neighbor PZTs in the designed network. However,  
54  $A_0$  mode can be more appropriate since it allows an interaction with a delamination at smaller excitation  
55 frequencies than  $S_0$  mode and has been favored in most recent works [10–12]. Actually, both modes can  
56 be used as long as the excitation frequency chosen (and the resulting wavelength of each mode) allow  
57 an interaction with the damage [9, Para. 19.5.2.2]. Common methods used to study the behavior of a  
58 given mode ( $A_0$  or  $S_0$ ) are based on response signal obtained with collocated transducers [9, Ch. 17], or  
59 the use of “sweet spot frequencies” [13, Ch. 8] where only one mode is generated. The former method  
60 requires having access to both sides of the instrumented structure and a perfect collocation of the  
61 transducers, and the latter restrains the application to specific excitation frequencies that may not  
62 correspond to the damage size to detect. Those limitations are overcome by dual PZTs. Dual PZTs are  
63 made of a concentric ring and disc as shown in figure 1. Both parts can be used as actuators and sensors  
64 bringing more signal combinations than conventional PZTs and allow for the isolation of the first  
65 antisymmetric  $A_0$  or symmetric  $S_0$  mode. With dual PZTs, a damage can then be detected in a “*baseline-*  
66 *free*” manner by using the damage-introduced mode conversion and attenuation (which is not the same  
67 for each mode) of the propagating waves [8]. The theoretical aspect justifying the use of those PZTs for  
68 “*baseline-free*” SHM (BF-SHM) is well developed in [18] and experiments are reported in [19] on  
69 aluminum and in [20] on composite structures. However, the interaction of each mode with the damage  
70 is conditioned by the wavelength of the waves generated by the dual PZT and the damage dimension.  
71 As a consequence, the transducer’s dimensions as well as excitation frequencies must be chosen with  
72 care. The first objective of the present work is to propose a method for dual-PZT sizing and excitation  
73 frequency selection according to the targeted application, *i.e.* BF-SHM. Furthermore, previous works  
74 with dual PZTs have been carried out on quasi-isotropic structures but, to our knowledge, no studies  
75 have been reported on anisotropic structures. In such materials, the amplitude as well as the propagation  
76 speed of  $A_0$  and  $S_0$  modes on a path between two PZTs depends on the angle between the path direction  
77 and the orientation of the carbon fibers composing the structure [9]. Since the mode decomposition  
78 method depends on the amplitude ratio between both modes, the PZT positions (in terms of distance and  
79 orientation) need to be chosen carefully to guarantee a sensibility of both modes in any configuration.

80 The second objective of the present work is then to propose a method to determine the optimal distance  
81 and orientation between neighbor dual-PZTs. Another underlying objective is to optimize the number  
82 of active elements which is a key point for industrial deployment specially in aeronautical applications



83

**Figure 1** : Simplified view of a dual PZT composed of a concentric ring and a disk.

84 Some of the BF-SHM methods, where mode decomposition using dual PZT is of interest, are here  
85 quickly reviewed. The “*instantaneous baseline*” method is based on a transducer network with paths  
86 having the same dimensions and orientations. Instead of comparing signals obtained at unknown  
87 conditions with a pristine baseline, signals are compared instantaneously between paths even under  
88 varying environmental conditions [15, 21–24]. Drawbacks concern examined paths that must have  
89 identical PZT positioning and bonding and avoidance of elastic waves reflections from boundaries.  
90 Another technique called the “*time reversal*” process assumes that for a pristine structure by sending  
91 back the reverse signal received by a given PZT, the input signal used in first place should be recovered.  
92 A damage potentially breaks this relation, allowing for its detection. This method has been validated on  
93 composite structures [11, 25–28] and its limitations have been identified [29]: a high dependency on the  
94 excitation frequency, mode dispersion, and reflections from boundaries. In the “*reciprocity principle*”  
95 method, two signals obtained from both possible directions of a given path are directly compared. This  
96 method has been used successfully in aluminum [15, 19, 30] and quasi-isotropic composite [12]  
97 structures. Its drawbacks are that the implemented PZTs must be identically bonded to the structure, and  
98 that damages localized far from the investigated path are difficult to detect.

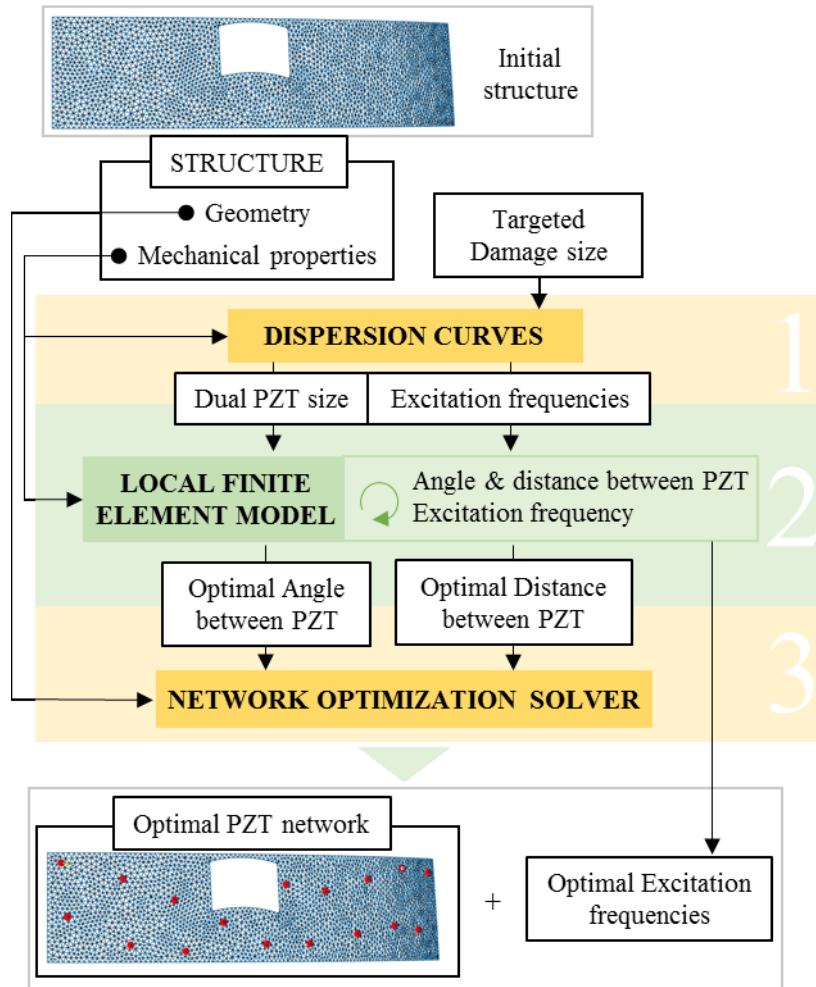


Figure 2: Different steps for the optimal design of a dual-PZT network on an anisotropic composite structure.

99 BF-SHM studies focus on the description of damage detection methods, but do not address the problem  
 100 of network design when dealing with large structures. However, the PZT network (size, number,  
 101 distance, and orientation of transducers as well as excitation frequency) to be used highly depends on  
 102 the considered damage detection method, the environmental conditions, and the geometry of the  
 103 structure. This step must thus be considered with great care. There have been studies on Optimal Sensor  
 104 Placement (OSP) for reference-based Lamb-wave based SHM applications [31–36] with recent focus  
 105 on composite structures [36–38]. These studies show that relevant criteria for PZT positioning are the  
 106 distance between two neighbor PZTs and the presence of complex geometries [37] (large holes,  
 107 stiffeners...) on paths between PZT. In BF-SHM applications, additional and very restrictive constraints  
 108 on PZT networks exist. Based on the observations described above, the current work proposes an

109 original three-step process to design an optimal dual-PZT network for a structure to be monitored by  
 110 means of BF-SHM methods. As depicted in figure 2, the different steps of this process are:

- 111 1. The mechanical properties of the structure are used to compute the dispersion curves of Lamb  
 112 waves in the investigated material. Dispersion curves and the minimal size of the damage to be  
 113 detected allow sizing dual-PZTs and determining excitation frequencies of interest.
- 114 2. A local FEM model (a plate corresponding to a small part of the monitored structure) equipped  
 115 with two dual-PZTs is used. Lamb wave attenuation with distance  $r$  and orientation  $\theta$  and for  
 116 different excitation frequencies  $f_0$  is extracted. Two original indexes quantifying the ability of  
 117 the set  $(f_0, r, \theta)$  for mode decomposition are then computed. This provides optimal parameters  
 118  $(\hat{f}_0, \hat{r}, \hat{\theta})$  for neighbor dual-PZTs of the network.
- 119 3. The network optimization solver applies the optimal parameters obtained from the local FEM  
 120 model to the real structure to propose a candidate optimal dual-PZT configuration.

121 The rest of the paper is organized as follows, in section II, the material and geometry of the targeted  
 122 aeronautical structure under study are presented. Then in section III, each step of the process is described  
 123 and illustrated with results obtained on a highly anisotropic composite material. Finally, in sections IV  
 124 and V, PZT networks obtained for different geometries and different composite materials are displayed,  
 125 analyzed and discussed.

## 126 2. Material and structure under study

127 Composite materials are of great interest in an aeronautical context since they provide lighter  
 128 structures having the same mechanical properties than previously used materials. The composite  
 129 material under study is a highly anisotropic composite fiber reinforced polymer (CFRP) with 16 plies  
 130 oriented at  $[0^\circ/90^\circ]$ . Mechanical properties of one ply are listed in table 1.

131 **Table 1:** Properties of a layer of the CFRP composite laminate.

$E_1$ [GPa]	$E_2 = E_3$ [GPa]	$\nu_{31}$	$\nu_{23} = \nu_{12}$	$G_{23} = G_{31}$ [GPa]	$G_{12}$ [GPa]	$\rho$ [kg. m <sup>-3</sup> ]
121	8.6	0.06	0.31	4.3	5.9	1520

132 A part of a nacelle from an A380 plane (the fan cowl as shown in figure 3) is considered to illustrate the  
 133 three-step process proposed to design an optimal dual-PZT network for BF-SHM methods. This  
 134 geometrically complex structure is 2.20 m in height for a semi circumference of 5.80 m and is made of  
 135 composite monolithic carbon epoxy material. Piezoelectric elements manufactured by NOLIAC (see  
 136 table 2) are used to trigger and collect Lamb waves in that structure.

137 **Table 2:** Electro-mechanical properties of the PZT material NCE51 from Noliac.

$E_{11}$ [GPa]	$E_{33}$ [GPa]	$\alpha$ [1/K]	$\nu$	$d_{31}$ [pC/N]	$d_{33}$ [pC/N]	$s_{11}^E$ . $10^{-12}$	$s_{33}^E$ . $10^{-12}$	$\rho$ [kg. m <sup>-3</sup> ]
62.50	52.63	$2 \cdot 10^{-6}$	0.38	-195.00	460.00	16.00	19.00	7600

138

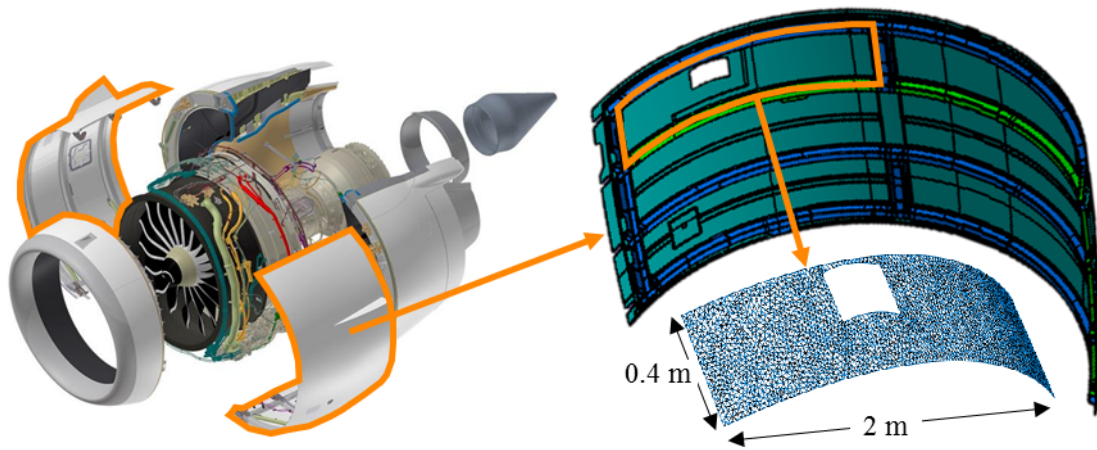


**Figure 3:** Aircraft nacelle (left), original fan cowl geometry and simplified 3D geometry of the subpart studied (right).

### 139 3. Optimal dual PZT sizing and placement

#### 140 1.1 PZT dimension and excitation frequency

141 In this first step of the proposed method, the dimensions of the PZT to be used as actuators and  
 142 sensors and the excitation frequencies are determined based on the material properties and on the  
 143 minimal size of the damage to be detected. This approach is developed to meet three main goals (see  
 144 figure 4):

- 145 (i) Only the first symmetric and antisymmetric modes  $S_0$  and  $A_0$  must be generated,
- 146 (ii) The dual PZT used as an actuator and the frequencies of the signal used must guarantee the
- 147 excitation of  $S_0$  and/or  $A_0$  modes with a wavelength small enough to interact with the
- 148 targeted minimal damage,
- 149 (iii) The dual PZT used as sensor must be sensitive to both  $S_0$  and  $A_0$  modes on the selected
- 150 range of excitation frequencies.

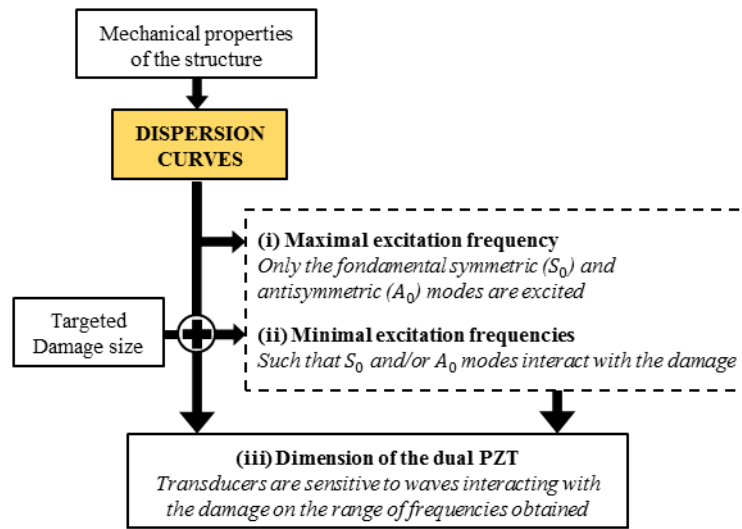


**Figure 4:** Schematic illustration of the three steps followed to select the dimensions of the dual PZT from dispersion curves. This corresponds to Step 1 in figure 2.

151 Dispersion curves are computed numerically by finding all the possible frequencies that satisfy Lamb

152 waves dispersion relations with iterations on the wave number  $k$  [39]. Once those values are computed,

153 the dispersion curves can be displayed as the variation of wavelength  $\lambda = 2\pi/k$  of each symmetric and

154 antisymmetric modes with frequency. Dispersion curves can also be computed for some rheological

155 materials (please refer to [40] for an open software). The dispersion curves displayed in figure 5 are

156 computed considering plane waves propagating in a homogenized material with the properties given in

157 table 3 corresponding to the  $0^\circ$  direction of a  $[0^\circ, 90^\circ]_{16}$  CFRP plate. The  $0^\circ$  orientation is chosen since

158 it is the direction where wavelengths are larger, hence a dual PZT dimensioned for those wavelength

159 will respect criteria described in figure 4 in all orientations.

160

161 **Table 3:** Mechanical properties of the  $[0^\circ, 90^\circ]_{16}$  homogenized CFRP plate

$E$ [GPa]	$\nu$	$\rho$ [ $\text{kg. m}^{-3}$ ]	$t$ [mm]
45.5	0.09	1600	2

162

163 BF-SHM methods targeted here consist in tracking  $S_0$  and  $A_0$  mode conversion and attenuation. It is  
 164 thus necessary to restrain the domain of applications where only those first two modes propagate.  
 165 Dispersion curves for higher frequencies (not displayed here) show that the excitation frequency should  
 166 not exceed  $f_{max} = 906$  kHz (corresponding in our case to the minimal excitation frequency for which  
 167 mode  $A_1$  is generated) to meet this condition. A second point to consider is that theoretically half the  
 168 wavelength  $\lambda$  of the wave used to detect a damage must be shorter than or equal to the size of the damage  
 169  $\phi_d$  in order to allow an interaction with it [41]:

$$\frac{\lambda}{2} \leq \phi_d \quad (1)$$

170 This leads us to bound the frequency range under which  $S_0$  and  $A_0$  can be exploited: the largest  
 171 wavelength validating equation (1) is  $\lambda_d = 2 \times \phi_d$ . According to this criterion, the excitation frequency  
 172 used should be greater than a frequency  $f_{A_0}$  for  $A_0$  mode and  $f_{S_0}$  for  $S_0$  mode, corresponding to excitation  
 173 frequencies for which wavelength  $\lambda_{A_0}$  and  $\lambda_{S_0}$  are lower than  $\lambda_d$ . (see figure 5). As advised by the  
 174 aeronautical manufacturer who provided the samples, the minimal damage size that must be detected  
 175 (BVID for Barely Visible Impact Damage) is 20 mm, hence in our case,  $\lambda_d = 40$  mm,  $f_{A_0} = 12$  kHz  
 176 and  $f_{S_0} = 134$  kHz (see figure 5).

177 Furthermore, it is mandatory to ensure that at these frequencies the dual-PZT element can actuate and  
 178 receive the desired modes. This then leads us to select optimal dual PZT dimensions. Two criteria are  
 179 important in the choice of the PZT according to [42]:

- 180 • as an actuator, the optimal PZT size  $\phi_{PZT}$  is obtained for

$$\phi_{PZT} = \lambda \left( n + \frac{1}{2} \right), \quad n = 0, 1, 2, \dots \quad (2)$$

181 • as a sensor, the sensitivity of the PZT increases as its size is reduced and the size of the PZT  
 182 must be inferior to half the wavelength to be detected, *i.e.*

$$\Phi_{PZT} \leq \frac{\lambda}{2} \quad (3)$$

183 When classic circular PZT are used as actuators and sensors, the optimal PZT size is obtained for  $\Phi_{PZT} =$   
 184  $\Phi_d$  by considering criteria described by equations (1), (2) and (3). However, this choice limits in practice  
 185 the application of detection to very few excitation frequencies. An advantage of the dual PZT, in addition  
 186 to its mode decomposition ability, is that both parts of the PZT can be chosen independently.  
 187 Nevertheless, as the disk part of the dual PZT is also used as an actuator for the mode decomposition  
 188 process, it should not be too small to allow the generation of Lamb waves. The choice of ring part  
 189 dimension of the dual PZT,  $\Phi_{PZT-ring}$  is chosen such that the maximum energy (see equation (2) with  
 190  $\lambda = \lambda_d$  and  $n = 0$ ) is communicated to the structure for the targeted minimal damage size. According  
 191 to [42], the equivalent diameter for a ring PZT  $\Phi_{PZT-ring}$  can be determined as the outer diameter minus  
 192 the inner diameter *i.e.*

$$\Phi_{PZT-ring} = \Phi_{PZT-ring}^{outer} - \Phi_{PZT-ring}^{inner} = \Phi_d \quad (4)$$

193 In our case, it gives  $\Phi_{PZT-ring} = 20$  mm. The choice of the central part dimension of the dual PZT  
 194  $\Phi_{PZT-disk}$  is governed by the range of frequencies on which BF-SHM methods will be investigated. In  
 195 the case presented in figure 5, it is interesting to have sensors sensitive to both modes for frequencies  
 196 up to  $f_{S_0}$  because it is the smallest frequency for which both modes are activated and interact with the  
 197 targeted damage size. To guarantee the sensitivity of the  $A_0$  mode at this frequency, the dimension of  
 198 the central part of the dual PZT should be sensible to wavelength equal to  $\lambda_{min} = \lambda_{A_0}(f_{S_0})$  (wavelength  
 199 of mode  $A_0$  obtained at  $f_{S_0}$ , see figure 5). Using equation (3), this dimension of the disk is obtained for:

$$\Phi_{PZT-disk} = \lambda_{A_0}(f_{S_0})/2 \quad (5)$$

200 In the current application,  $\lambda_{min} = 11$  mm, hence  $\Phi_{PZT-disk} = 5.5$  mm.

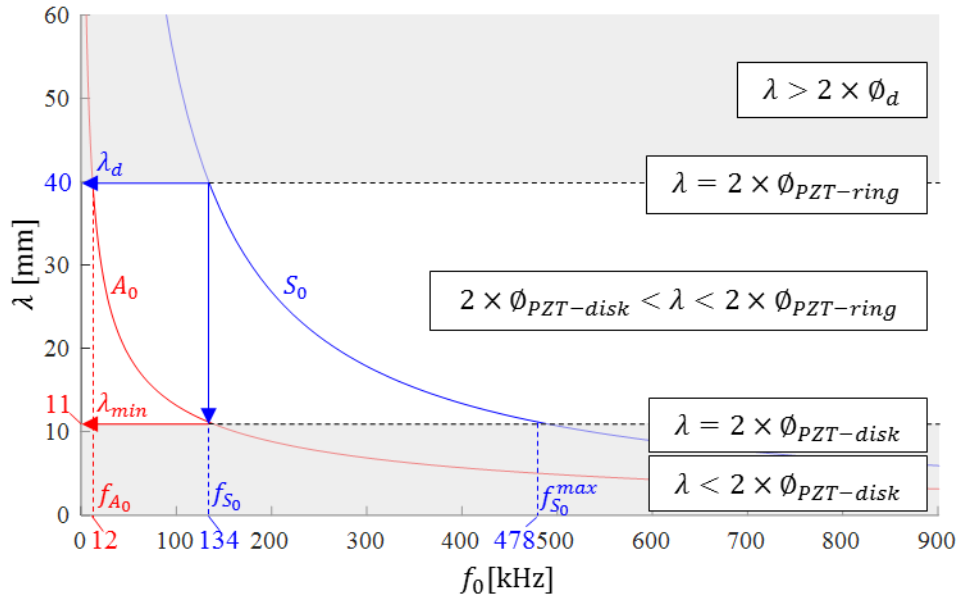


**Figure 5:** Dispersion curves for material described in table 3. It shows the minimum frequency to use ( $f_{A_0} = 12$  kHz for  $A_0$  mode and  $f_{S_0} = 134$  kHz for  $S_0$  mode) to allow for an interaction between the propagating wave and a damage of size  $\phi_d = 20$  mm. It also shows the range of frequencies to use to guarantee a sensitivity of the dual PZT to  $A_0$  mode and  $S_0$  mode for frequencies up to  $f_{S_0} = 134$  kHz. The disk part of the dual-PZT is also sensible to  $S_0$  mode up to  $f_{S_0}^{max} = 478$  kHz.  $\phi_{PZT-disk} = 5.5$  mm and  $\phi_{PZT-ring} = \phi_d = 20$  mm.

201 Figure 5 highlights four distinguishable areas:

- 202
- $0 < f_0 < f_{A_0}$ : the dual PZT triggers  $A_0$  mode but it does not interact with the damage
- 203
- $f_{A_0} < f_0 < f_{S_0}$ : the dual PZT triggers  $A_0$  and  $S_0$  modes but only  $A_0$  mode interacts with the
- 204 damage. Both modes can be properly measured by the disk part of the dual PZT, but the ring
- 205 part is theoretically only sensitive to the  $S_0$  mode.
- 206
- $f_{S_0} < f_0 < f_{S_0}^{max}$ : the dual PZT triggers  $A_0$  and  $S_0$  modes and both modes interact with the
- 207 damage, but only  $S_0$  mode can be properly measured by the disk part of the dual PZT, and the
- 208 ring part is theoretically insensitive to any mode.
- 209
- $f_0 > f_{S_0}^{max}$ : the dual PZT triggers  $A_0$  and  $S_0$  modes and both modes interact with the damage,
- 210 but the PZT is not sensitive to any mode.

211 According to the PZT manufacturer (NOLIAC), the gap between the two electrodes designed on the  
212 upper surface of the PZT should not be less than 1 mm. Following this instruction and equations (4) and  
213 (5) the dual PZT dimension must respect:

$$214 \quad \phi_{PZT-disk} \leq \lambda_{A_0}(f_{S_0})/2$$

$$215 \quad \phi_{PZT-ring}^{inner} \geq \phi_{PZT-disk} + 2 \text{ mm}$$

$$216 \quad \phi_{PZT-ring}^{outer} = \phi_{PZT-ring}^{inner} + \phi_d$$

217 The smallest dual PZT that satisfies all those recommendations is obtained for  $\phi_{PZT-disk} = 5.5$  mm,  
218  $\phi_{PZT-ring}^{inner} = 7.5$  mm and  $\phi_{PZT-ring}^{outer} = 27.5$  mm. The associated excitation frequency range of interest  
219 is from 12 to 134 kHz because it allows mode conversion tracking for both modes while guaranteeing  
220 an interaction of the propagating Lamb waves with the damage.

### 221 3.2 Optimal distance and orientation between neighbor PZTs of the network

222 Two important information not provided by dispersion curves are the attenuation of waves  
223 propagating within the material and the efficiency with which both Lamb wave modes are converted to  
224 electric signals by the dual-PZT. In anisotropic materials, the attenuation varies a lot with the distance  
225 and the orientation of the fibers, and symmetric and antisymmetric modes are not identically affected.  
226 This is rarely considered in the design of the PZT network whereas it is of great importance to estimate  
227 optimal relative placement of neighbor PZTs, as illustrated in figure 6. The analysis of the  
228 electromechanical efficiency of the dual-PZT will be useful to assess the mode decomposition abilities  
229 of the chosen PZT and to validate the ability of the network to be used in a BF-SHM manner.

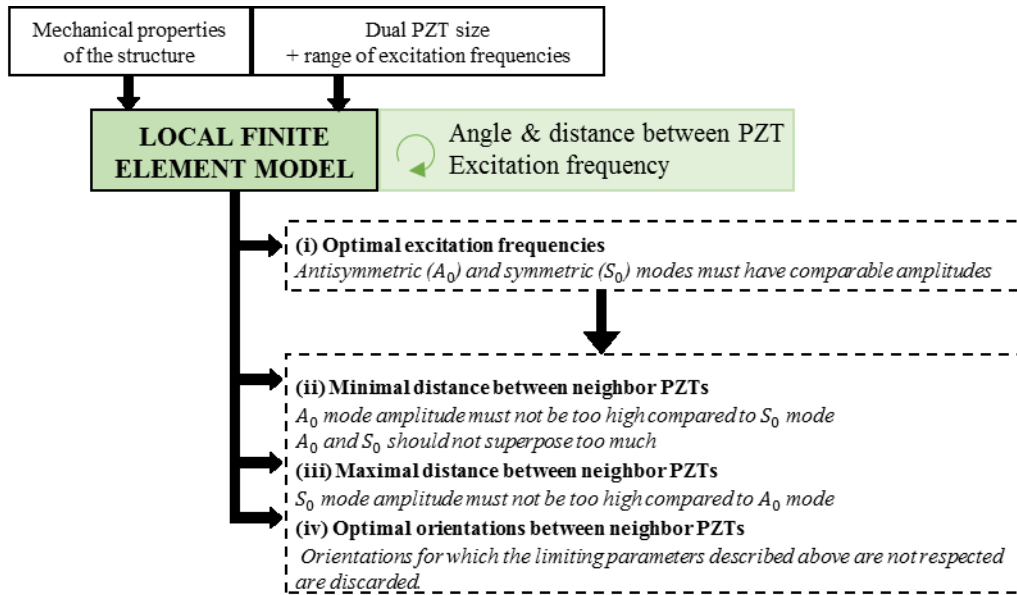


**Figure 6:** Schematic illustration of inputs and outputs to the local FEM (Step 2 of figure 2) as well as limiting parameters for the optimal placement of neighbor PZTs and excitation frequencies.

### 230 3.2.1 Local Finite Element Model representative of the structure

231 A local FEM model is built using SDTools® [43]. This model is local in the sense that it corresponds  
 232 only to a FEM model of a rectangular plate made up of the same material as the whole structure instead  
 233 of a FEM model of the complete structure (see figure 7 and table 2). This local approach aims at  
 234 diminishing the number of nodes of the FEM model and provide an affordable simulation in terms of  
 235 computation time. It is necessary in a context where parametric studies are conducted with transient  
 236 simulations performed at various excitation frequencies. Quadratic elements with dimension  $2\text{ mm} \times$   
 237  $2\text{ mm}$  are used for the meshing of the plate. This mesh size is compatible with the wavelength of  $A_0$   
 238 and  $S_0$  modes which value does not exceed  $11\text{ mm}$  on the investigated frequency range and has been  
 239 validated by a convergence test. The excitation signal is chosen as a 5 cycles sinusoidal tone burst  
 240 modulated by a Hanning window at an amplitude of  $10\text{ V}$  and a central frequency  $f_0$  varying from  $10$  to  
 241  $140\text{ kHz}$  (average interval from  $f_{A_0}$  to  $f_{S_0}$  in figure 5) by steps of  $10\text{ kHz}$ . For each step, simulations are  
 242 conducted alternatively with each possible emission scheme (entire PZT, ring part, disk part), leading  
 243 to a total of  $30$  simulations. The time step for the transient simulation is  $0.36\text{ }\mu\text{s}$  and corresponds to a  
 244 sampling frequency of  $2.8\text{ MHz}$ . The transient simulation is performed with Newmark's method and

245 the structure dynamic damping is simulated by considering a coefficient of  $5.10^{-8}$  for the stiffness  
 246 matrix and no damping coefficient for the mass matrix (coefficients obtained from a calibration with  
 247 experimental measurements and used in [44]). The plate used for the simulation is a  $[0^\circ, 90^\circ]_{16}$  CFRP  
 248 plate with the properties given in table 1 modeled as a 3D orthotropic material and homogenized using  
 249 Mindlin theory for thin laminate plates. The PZT elements are composed of Noliac NCE51 material (see  
 250 properties in table 2) and simulated as piezoelectric shell finite elements. The inter-distance between  
 251 PZTs is 400 mm and the circle arc to study attenuation with orientation is placed 150 mm away from  
 252 the actuator. Previous works, using this software, have been conducted to assess SDTools® proposed  
 253 PZT elements reliability for SHM applications. Indeed, the electromechanical interaction and the effect  
 254 of glue and temperature have been experimentally validated [45, 46]. The displacement is saved for each  
 255 node between the actuator and the sensor to estimate Lamb wave attenuation with distance, and on the  
 256 circle around the actuator to estimate Lamb wave attenuation with orientation (see figure 7).

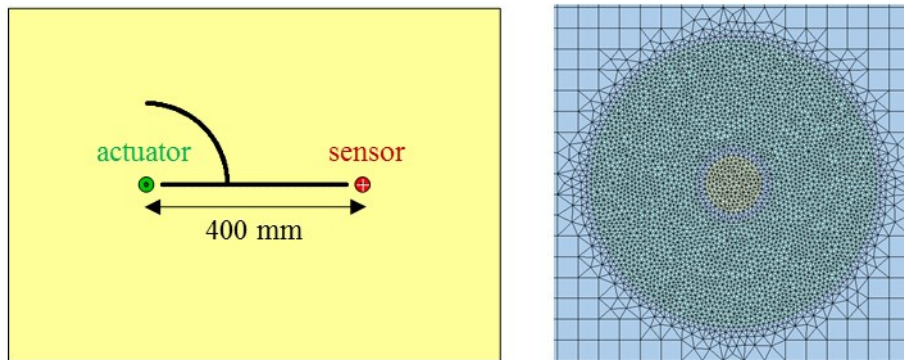


**Figure 7:** Local FEM composite plate with two dual PZTs and the sensing point (black line and circle) used to study antisymmetric and symmetric mode propagation (left) and mesh of the dual PZT (right)

### 257 3.2.2 Lamb waves attenuation and dual-PZT electromechanical efficiency

258 The electric signal measured by the dual PZT  $V_{a \rightarrow s}$ , depending on the PZT part used as actuator  $a$ ,  
 259 the PZT part used as sensor  $s$ , the distance  $r$  between actuator and sensor, the orientation compared to  
 260 the  $0^\circ$  ply  $\theta$  and the excitation frequency of the input  $f_0$  can be analytically expressed as:

261

$$V_{a \rightarrow s}(r, \theta, f_0, t) = V_{a \rightarrow s}^{A_0}(r, \theta, f_0, t) + V_{a \rightarrow s}^{S_0}(r, \theta, f_0, t) \quad (6)$$

$$V_{a \rightarrow s}^{[X]_0}(r, \theta, f_0, t) = C^{[X]_0}(r, \theta, f_0, t) \times S_{a \rightarrow s}^{[X]_0}(f_0) \quad (7)$$

262 where  $t$  is the time,  $V_{a \rightarrow s}^{A_0}$  and  $V_{a \rightarrow s}^{S_0}$  refer to the electrical signal measured by the PZT for  $A_0$  and  $S_0$  mode  
 263 when part  $a$  is used as actuator and part  $s$  is used as sensor.  $[X]$  is either  $A$  or  $S$  referring to antisymmetric  
 264 or symmetric mode.  $C^{[X]_0}$  is independent of the actuator or sensor size as shown in [18], and corresponds  
 265 to the mechanical displacement attributable to the  $[X]_0$  mode at the sensor position. In the approach  
 266 proposed here, the antisymmetric mode is assumed to correspond mainly to the out-of-plane  
 267 deformations and the symmetric mode to correspond mainly to the in-plane deformations.  $S_{a \rightarrow s}^{[X]_0}$  then  
 268 corresponds to the electromechanical efficiency of the PZT to mode  $[X]_0$  for actuator  $a$  and sensor  $s$ .  
 269 Since  $S_{a \rightarrow s}^{[X]_0}$  only depends on the excitation frequency  $f_0$ , it can be determined from the electrical signal  
 270 obtained on the dual PZT electrodes of the PZT sensor and the mechanical displacements measured at  
 271 the center of the sensor (the white cross in figure 7). With equations (6) and (7) and  $C^{[X]_0}(r, \theta, f_0, t)$   
 272 obtained from the FEM simulation,  $S_{a \rightarrow s}^{A_0}(f_0)$  and  $S_{a \rightarrow s}^{S_0}(f_0)$  are computed with an iterative process that  
 273 consists in finding the minimum mean square error between the envelope of the signal measured on the  
 274 PZT electrode  $V_{a \rightarrow s}(r, \theta, f_0, t)$  and the sum of envelopes of  $C^{A_0}(r, \theta, f_0, t) \times S_{a \rightarrow s}^{A_0}(f_0)$  and  
 275  $C^{S_0}(r, \theta, f_0, t) \times S_{a \rightarrow s}^{S_0}(f_0)$  (the iteration is performed on values of  $S_{a \rightarrow s}^{A_0}(f_0)$  and  $S_{a \rightarrow s}^{S_0}(f_0)$ ). Figure 10(b)  
 276 shows an example of envelopes of each mode displacements scaled by their respective  
 277 electromechanical efficiencies and the response signal measured by the disk part of the dual PZT.  
 278 Figure 8 shows the variation of electromechanical efficiency of ring and disk parts of the dual PZT for  
 279  $A_0$  and  $S_0$  mode depending on the excitation frequency. The disk part appears to be much more efficient  
 280 than the ring part to measure the  $A_0$  mode on the whole range of frequencies considered, whereas both  
 281 parts are efficient to measure the  $S_0$  mode. This graph echoes the results observed in figure 5 and the  
 282 associated observations. It also explains the ability of dual-PZTs to decompose modes in the measured  
 283 signal since each part of the dual PZTs exhibit different electromechanical efficiency for each mode.

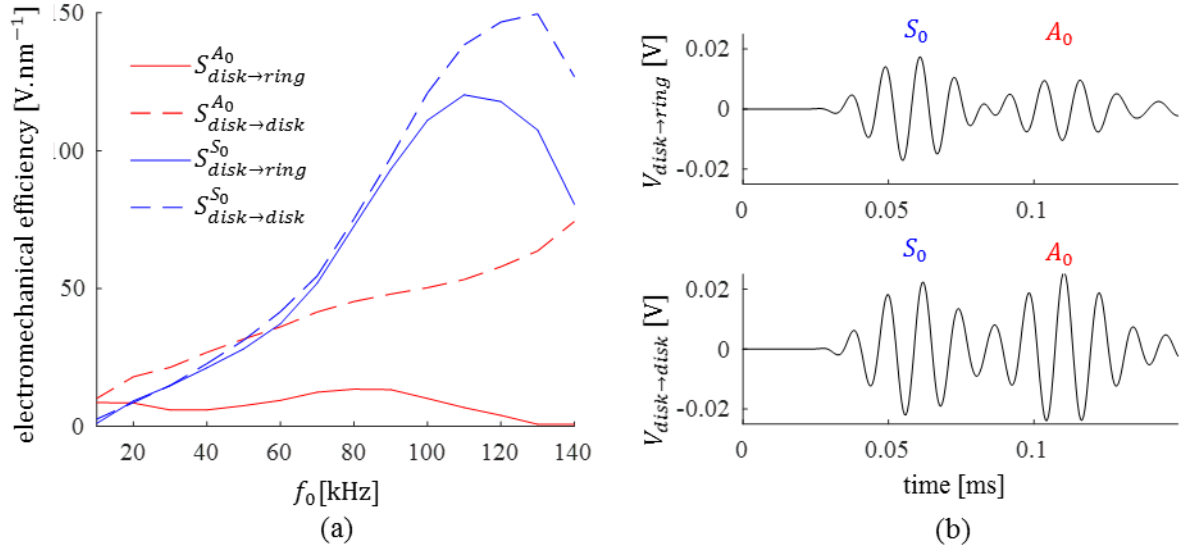


**Figure 8:** (a) Variation of electromechanical-efficiency of PZT sensor ring and disk for  $S_0$  and  $A_0$  mode against excitation frequency  $f_0$ . (b) Response signal obtained for  $r = 150$  mm,  $\theta = 0^\circ$ ,  $f_0 = 80$  kHz with the disk as actuator and the ring or the disk as sensor.

284 Figure 9(a) shows that  $A_0$  and  $S_0$  have different amplitude variation with excitation frequency:  $A_0$  mode  
 285 is significantly greater for lower frequencies (below 35 kHz) whereas  $S_0$  mode is greater for higher  
 286 frequencies (after 90 kHz). Figure 9(b) shows that  $A_0$  mode attenuates faster than  $S_0$  mode with distance.  
 287 From figure 10(a) one can see that  $S_0$  is much more impacted by the wave propagation direction than  
 288  $A_0$ . The  $S_0$  mode tends to propagate well in the composite fibers directions (maximum at  $0^\circ$  and  $90^\circ$ )  
 289 but its amplitude can be reduced to 10 % of its maximum value (around  $17^\circ$  and  $73^\circ$ ). The  $A_0$  mode  
 290 amplitude (maximum at  $0^\circ$ ) is only reduced to 50% of its maximum value at  $45^\circ$ . Figure 10 emphasizes  
 291 the fact that, both modes may have the same amplitudes in the  $0^\circ$  direction, but this comparison varies  
 292 a lot with the direction of propagation.

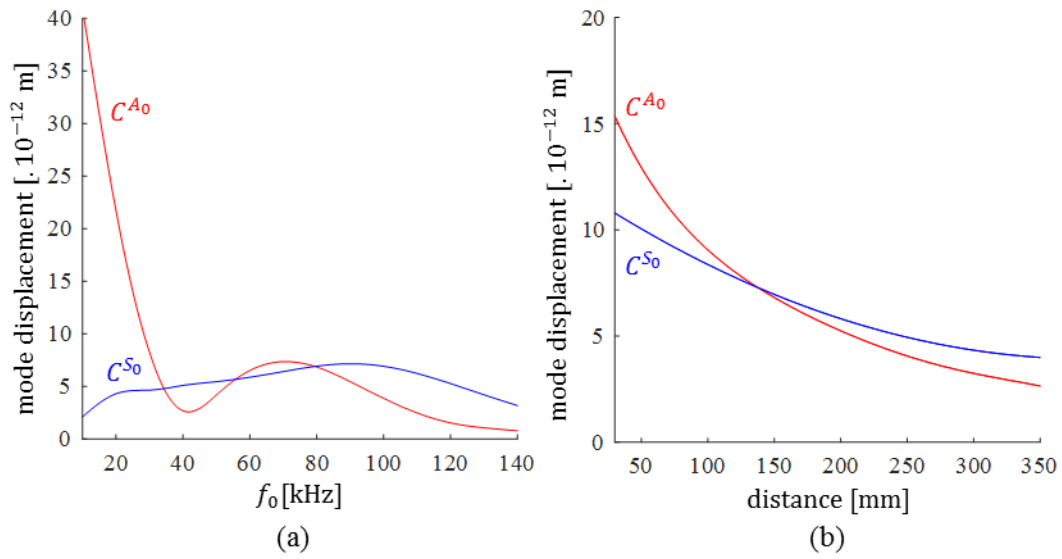


**Figure 9:** (a) Maximum amplitude variation of out-of-plane ( $\sim A_0$ ) and in-plane ( $\sim S_0$ ) displacement with frequency 150 mm away from the actuator in the  $0^\circ$  direction. (b) Maximum amplitude variation of out-of-plane ( $\sim A_0$ ) and in-plane ( $\sim S_0$ ) displacement with distance for  $f_0 = 80$  kHz in the  $0^\circ$  direction.

293

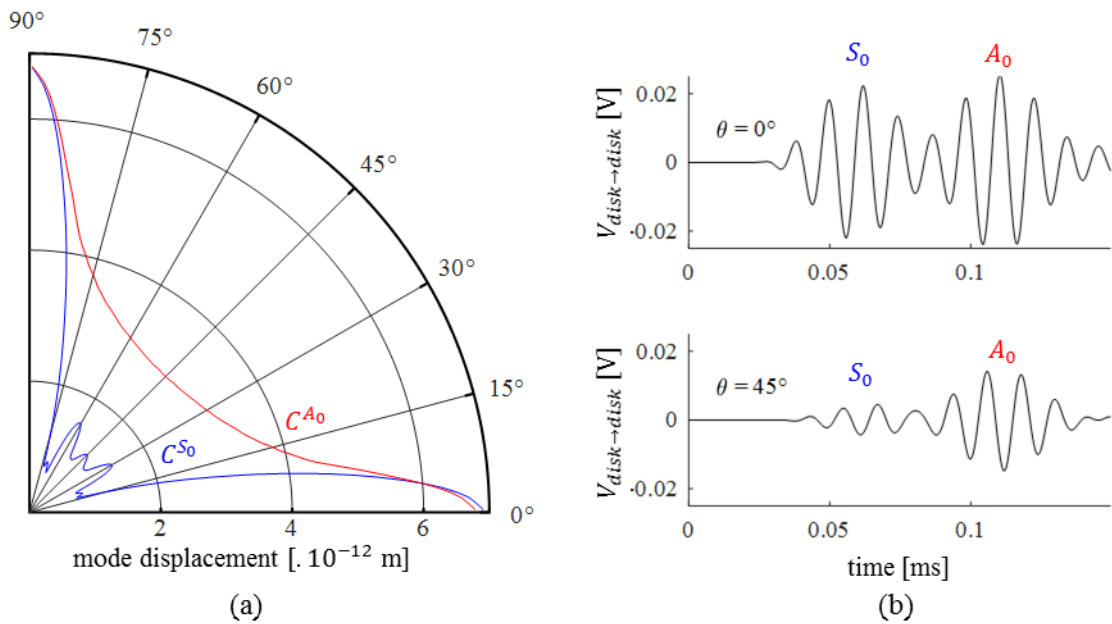


**Figure 10:** (a) Maximum amplitude variation of out-of-plane ( $\sim A_0$ ) and in-plane ( $\sim S_0$ ) displacement with orientation for  $f_0 = 80$  kHz and at a distance of 150 mm from the actuator. (b) Response signal measured by the disk part of the dual PZT for  $f_0 = 80$  kHz, at  $r = 150$  mm and  $\theta = 0^\circ$  or  $\theta = 45^\circ$ .

294 3.2.3 Optimal frequencies for mode conversion using dual PZT

295 In a BF-SHM context where  $A_0$  and  $S_0$  mode conversion and attenuation in presence of damage are  
 296 investigated [10, 16, 18, 47, 48], distance between neighbors dual-PZTs and orientation of the dual PZT  
 297 path with respect to fiber orientation as well as frequency of excitation must be correctly chosen such  
 298 that:

- 299 (i) The two modes propagate and are measured in comparable proportions,  
 300 (ii) The first wave packet of the  $A_0$  mode must not superpose too much with the  $S_0$  mode.

301 To evaluate those two parameters, two criteria are proposed:

$$\tilde{V}_{a \rightarrow s}^{A_0/S_0}(r, \theta, f_0) = \frac{\max \left[ \text{env} \left( V_{a \rightarrow s}^{A_0}(r, \theta, f_0, t) \right) \right]}{\max \left[ \text{env} \left( V_{a \rightarrow s}^{S_0}(r, \theta, f_0, t) \right) \right]} \quad (8)$$

$$\tau_{a \rightarrow s}(r, \theta, f_0) = \frac{\int_{t_0}^{t_1} \text{env} \left( V_{a \rightarrow s}^{A_0}(r, \theta, f_0, t) \right) + \int_{t_1}^{t_2} \text{env} \left( V_{a \rightarrow s}^{S_0}(r, \theta, f_0, t) \right)}{\int_{t_0}^{t_3} \text{env} \left( V_{a \rightarrow s}^{A_0}(r, \theta, f_0, t) \right)}, \quad (9)$$

302 where  $\text{env}(\cdot)$  denotes the envelope of the signal.  $[t_0, t_3]$  is the time interval corresponding to the first  
 303  $A_0$  wave packet,  $t_1$  the instant when  $V_{a \rightarrow s}^{A_0}$  gets higher than  $V_{a \rightarrow s}^{S_0}$ , and  $t_2$  the end of the first  $S_0$  wave  
 304 packet (see figure 12(b)).  $\tilde{V}_{a \rightarrow s}^{A_0/S_0}$  represents the amplitude ratio of the contribution of the  $A_0$  mode against  
 305 the contribution of the  $S_0$  mode in the measured response signal.  $\tau_{a \rightarrow s}$  qualifies the superposition of  
 306 modes in the measured response signal: it represents the intersection of both modes against  $A_0$  mode  
 307 measured in the time corresponding to the first  $A_0$  wave packet (see figure 12(b)). These two criteria  
 308 depend on the distance between actuator and sensor  $r$ , the orientation of the path actuator-sensor in  
 309 comparison with the  $0^\circ$  ply of the structure  $\theta$ , and the excitation frequency  $f_0$ . The PZT part chosen as  
 310 actuator has very little influence on the criteria chosen since it affects both modes amplitudes  
 311 proportionally. And as the disk part of the dual PZT is sensible to both  $A_0$  and  $S_0$  modes (in opposition  
 312 to the ring part), only results obtained with the disk part as actuator and sensor are displayed.

313 We introduce two thresholds  $\varepsilon_{\tilde{V}}$  and  $\varepsilon_{\tilde{\tau}}$  to determine whether a sensor position and excitation frequency  
 314 can be considered as suitable for mode decomposition. These thresholds will serve as tuning parameters  
 315 of the proposed method. The amplitude ratio of the  $A_0$  mode against the  $S_0$  mode as described in equation

316 (8) is used to select optimal frequencies where both modes are in comparable proportion in the response  
 317 measured by the disk part of the PZT. The threshold  $\varepsilon_{\tilde{V}}$  is set to 1/3 so that the amplitude of the  $A_0$   
 318 mode should not exceed 3 times the amplitude of the  $S_0$  mode and vice versa. Figure 11(a) shows the  
 319 maximum amplitude of each mode contribution obtained with equation (7) for the disk part of the dual  
 320 PZT at 150 mm from the actuator (the electromechanical efficiency of the sensor according to frequency  
 321  $S_{a \rightarrow s}^{[X]_0}$  is considered). The striped area depicts the frequency range for which the amplitude ratio does not  
 322 respect the threshold ( $\tilde{V}_{a \rightarrow s}^{A_0/S_0} > 1/\varepsilon_{\tilde{V}}$ ). Hence, the optimal frequency range to observe mode  
 323 conversion is from 40 to 140 kHz. This graph also shows that the optimal frequencies for  $A_0$  mode  
 324 studied alone would be for frequencies below 40 kHz because the amplitude of the  $A_0$  mode is  
 325 significantly higher than the  $S_0$  mode. 30 kHz corresponds to the “sweet spot frequency” of the  $A_0$  mode  
 326 in mode tuning methods. Those methods consist in an appropriate selection of the excitation frequency  
 327 of Lamb waves in order to generate only one of the Lamb wave modes [13, Para. 8.8]. The frequency  
 328 range obtained here is for the  $0^\circ$  orientation and is discussed for other orientations later. Figure 11(b)  
 329 shows the contribution of each mode on the measured response signal. A difference between the  
 330 maximum amplitude of the response signal ( $V_{disk \rightarrow disk}$ ) on wave packets corresponding to  $S_0$  (first wave  
 331 packet) and  $A_0$  (second wave packet) and the maximum amplitudes of each mode contribution  
 332 ( $V_{disk \rightarrow disk}^{A_0}$  and  $V_{disk \rightarrow disk}^{S_0}$ ) is noticed because a little mode conversion (from  $S_0$  to  $A_0$ ) occurs at the  
 333 edge of the ring part of the PZT and is measured by the disk part.

334

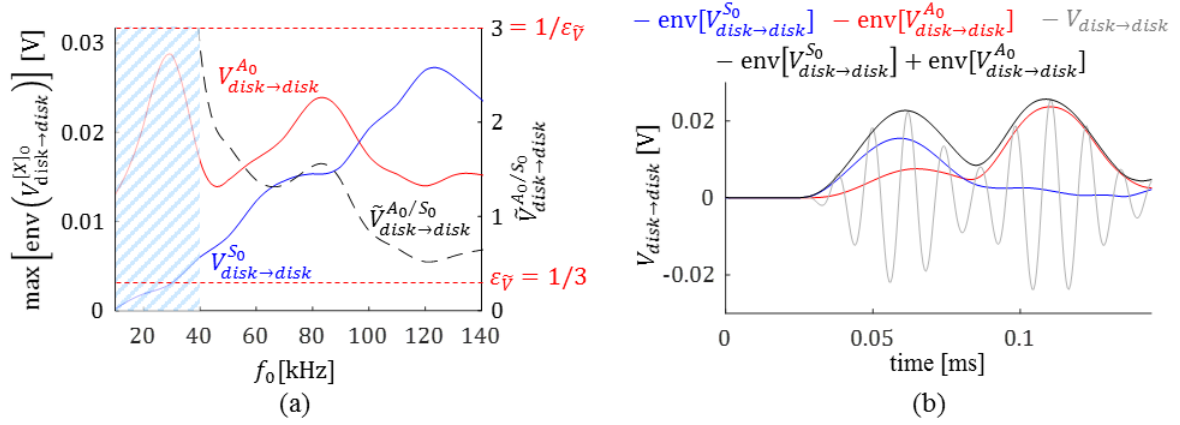


**Figure 11:** (a) Maximum amplitude of  $V_{disk \rightarrow disk}^{A_0}$  and  $V_{disk \rightarrow disk}^{S_0}$  in the response signal measured by the disk part of a dual PZT place for  $r = 150$  mm. The striped area represents the frequency range where the amplitude ratio  $\tilde{V}_{a \rightarrow s}^{A_0/S_0}$  (right axis) between maximum amplitude of  $V_{disk \rightarrow disk}^{A_0}$  and  $V_{disk \rightarrow disk}^{S_0}$  does not respect the threshold  $\varepsilon_{\tilde{v}} = 1/3$ . (b) Superposition of contributions of each mode and the signal measured by the disk part of the dual PZT for  $f_0 = 80$  kHz, at  $r = 150$  mm and  $\theta = 0^\circ$ .

### 335 3.2.4 Optimal distance and orientation between neighbor dual-PZTs

336 The minimum distance is obtained by observing the superposition  $\tau$  described in equation (9).  
 337 Results displayed in figure 12(a) show that a minimum distance  $r_{min}$  of 150 mm must be respected to  
 338 avoid superposition of the modes in the chosen excitation frequency range, and the superposition  
 339 threshold  $\varepsilon_{\tilde{\tau}}$  is set to 5% based on decomposition algorithm results observations. This allows us to  
 340 clearly distinct between  $S_0$  and  $A_0$  modes.

341

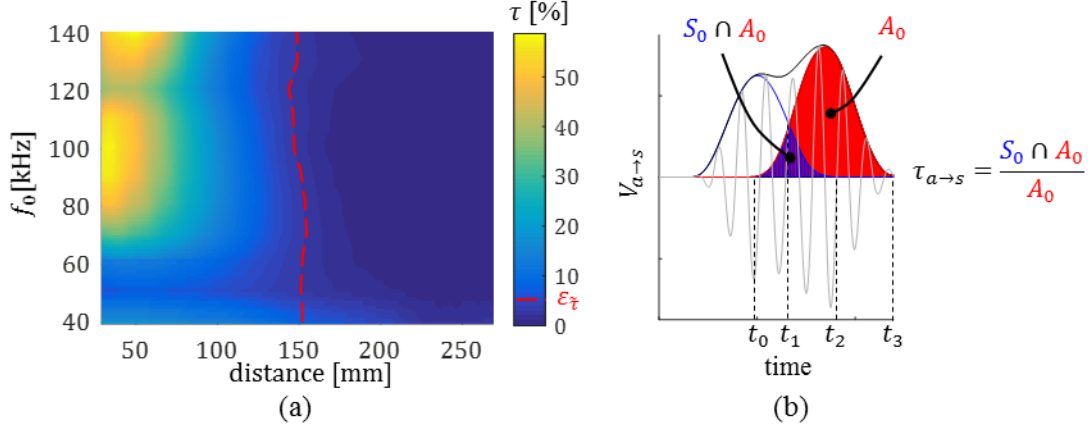


**Figure 12:** (a) Mode superposition against distance and excitation frequency for direct contribution of Lamb waves propagating in the  $0^\circ$  direction of a composite plate measured by the disk part of the dual PZT. (b) Representation of the superposition criteria estimation (equation (9)).

342 Given the orientation of the plies of the composite structure under study, it is relevant to notice that there  
 343 is a symmetry in the wave propagation such as propagation from  $0^\circ$  to  $45^\circ$  is exactly the opposite of the  
 344 propagation from  $90^\circ$  to  $45^\circ$  (this is observable on the results displayed in figure 10). First, from figure  
 345 10 (a), orientation  $17^\circ[\pi/2]$  and  $73^\circ[\pi/2]$  should be avoided since  $S_0$  mode hardly propagates in those  
 346 directions. Since  $A_0$  and  $S_0$  modes have different amplitude variations with frequency (see figure 9(a)),  
 347 distance (see figure 9(b)), and orientation (see figure 10), the amplitude criteria  $\tilde{v}_{a \rightarrow s}^{A_0/S_0}$  cannot meet the  
 348 threshold  $\epsilon_{\tilde{v}}$  for every excitation frequency, orientation and distance. Figure 13 shows the amplitude  
 349 ratio as measured by the disk part of the dual PZT for varying excitation frequencies and orientation. It  
 350 shows that for 150 mm (minimum distance for the superposition criteria), the threshold is exceeded for  
 351 excitation frequencies above 100 kHz and orientations  $10^\circ$  away from fiber directions. Except for an  
 352 excitation frequency of 40 kHz, this observation is not applicable for 300 mm (because  $A_0$  mode  
 353 attenuates faster than  $S_0$  mode, see figure 9(b)). However, at this distance the threshold is not respected  
 354 for frequencies higher than 130 kHz. Therefore, the range of frequencies is reduced to 50 to 140 kHz,  
 355 minimum distance between actuator and sensor  $r_{min}$  is evaluated at 230 mm (for shorter distance,  $A_0$   
 356 mode is too high compared to  $S_0$  mode at  $f_0 = 60$  kHz) and maximum distance  $r_{max}$  is evaluated at 270  
 357 mm (for larger distances,  $S_0$  mode is too high compared to  $A_0$  mode for  $f_0 = 140$  kHz and  $\theta = 0^\circ$ ).

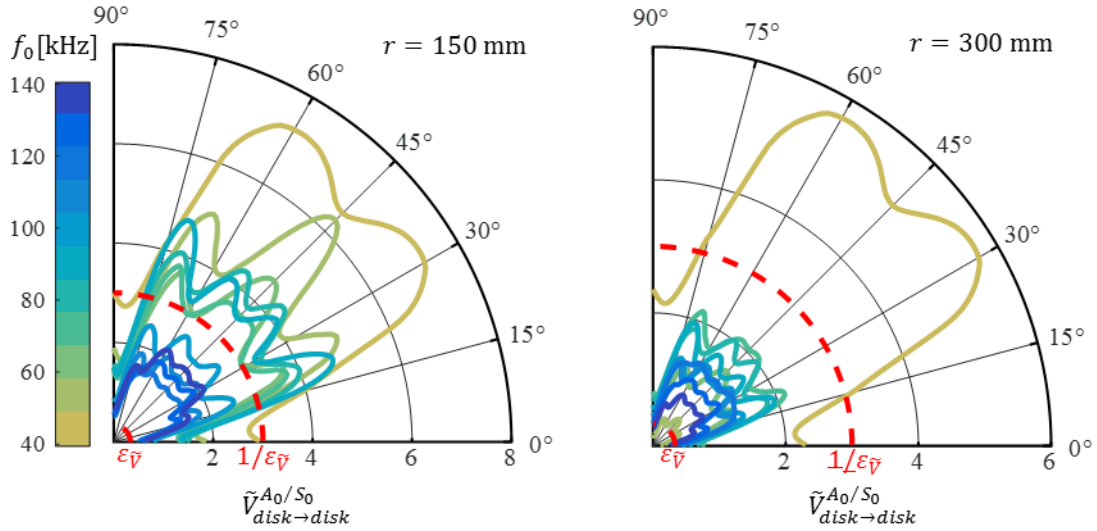


**Figure 13:** Amplitude ratio of the  $A_0$  mode against  $S_0$  mode amplitude and excitation frequency for  $r = 150$  mm and  $r = 300$  mm.

358 Figure 13 shows that the amplitude ratio at high frequencies is the limiting parameter for the maximum  
 359 distance between two PZT neighbors. On the one hand, having a larger range of frequencies enables to  
 360 robustify damage detection process (since damage indexes can be applied to several excitation  
 361 frequencies), and on the other hand, reducing the range of frequencies toward lower accepted values  
 362 lead to greater maximal distances  $r_{max}$ , which means fewer PZT on the targeted network. Hence, a  
 363 tradeoff between the robustness of the detection and the number of PZT is necessary.

### 364 3.3 PZT network optimization solver

365 The previous simulation step allows the determination of PZT placement requirements given by the  
 366 minimum and maximum distance between PZT ( $r_{min}$  and  $r_{max}$ ), and optimal angles of PZT paths  
 367 compared with the  $0^\circ$  orientation of the structure ( $\theta_{opt}$ ). Those requirements and the mesh of the  
 368 structure under study constitute the input parameters of the PZT network optimization as described in  
 369 the following algorithm:

370

### Algorithm: PZT placement

*Step 1:* First PZT node is randomly selected

- A node of the mesh is randomly selected and validated as the first PZT position

*End*

*Step 2:* Other PZT nodes are chosen

- One PZT node is selected as the reference node from the nodes already validated as PZT positions.
- All the nodes respecting the requirements (eligible nodes) are determined. To be selected, a node must:
  - (i) respect a distance at least equal to  $r_{min}$  from all the validated PZT positions
  - (ii) respect a distance at most equal to  $r_{max}$  with the node selected as reference
  - (iii) respect an orientation belonging to the optimal angles  $\theta_{opt}$  with the node selected as reference.
- One node is randomly selected among nodes respecting the requirements and added to the validated PZT positions. Eligible nodes common to multiple PZT nodes and farthest node from existing PZT nodes are favored.

*End*

*Step 3:* The algorithm stops

- The distance between each node of the mesh and the validated PZT positions is computed.
- If each node of the mesh is at a distance lower than  $r_{max}$  of any PZT, the algorithm stops. Else, it returns to step 2.

*End*

371

372 This approach may appear basic compared to other studies focusing on network optimization but allows  
373 for a simple transition from a local model to a larger structure. A constraint on boundary conditions is  
374 also considered to avoid border reflection influence on measured signals. Figure 14 shows the solver  
375 process for the selection of the first 3 PZT nodes respecting  $r_{min}$ ,  $r_{max}$  and  $\theta_{opt}$ . The “forbidden”

376 orientation refers to orientations  $17^\circ[\pi/2]$  and  $73^\circ[\pi/2]$ , corresponding to orientation not contained in  
 377  $\theta_{opt}$ . It is important to notice that the placement requirements are constrained by the capability of two  
 378 neighbor PZTs to allow mode decomposition on the path they form: if a dual PZT is placed in a  
 379 “forbidden orientation” (see figure 14), the decomposition process may be difficult to apply. However,  
 380 a damage in this zone will always interact with the propagating waves (at least with the  $A_0$  mode since  
 381 it is less influenced by plies orientations than the  $S_0$  mode, and is generated on all the given excitation  
 382 frequency range with wavelength allowing an interaction with the targeted damage size), hence the  
 383 influence of the damage on both modes will still be measured by the dual PZT path. In an aeronautical  
 384 context, the minimum number of transducers should be observed for weight purposes. In practice, the  
 385 algorithm considers this by taking a minimal distance which is close to  $r_{max}$  instead of  $r_{min}$ .

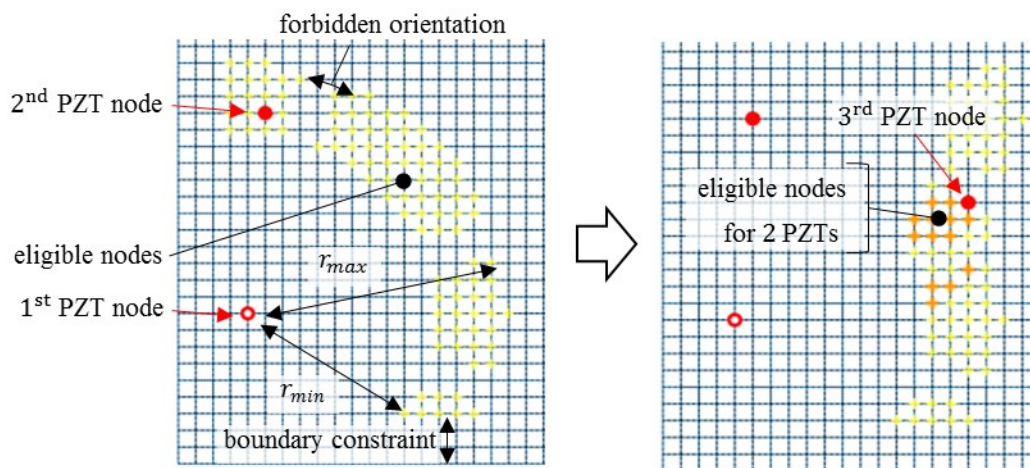


**Figure 14:** Illustration of the solver parameters and PZT node selection process. The optimization solver chooses nodes that are optimal for the maximum number of PZT nodes available.

## 386 4. Results

### 387 4.1 Tested cases

388 Four different cases (described in table 4) are considered in order to show the applicability of the  
 389 process to different structures. These cases are considered to show the influence of the anisotropy of the  
 390 material on the PZT network proposed, and the implementation to 2D and 3D structures. Two different

391 geometries and three materials are used. The first geometry - called “Plate” - is a large plate of  $2000 \times$   
 392  $500 \times 2 \text{ mm}^3$ , and the second one is the geometry of the subpart from the fan cowl (see figure 3). Three  
 393 different materials are compared (see table 4). The first one is the highly anisotropic CFRP with 16 plies  
 394 oriented at  $[0^\circ/90^\circ]$ , used for structure #1 and #4. The second material is an isotropic material with  
 395 simplified properties as displayed in table 3 used for structure #2. The third one is a quasi-isotropic  
 396 CFRP with 16 plies oriented at  $[0^\circ/90^\circ/45^\circ/-45^\circ]$  and properties of each ply described in table 1  
 397 (same ply properties as structure #1 and #4).

398 Figure 15 shows the variations of amplitude of  $A_0$  and  $S_0$  modes with orientation depending on the  
 399 material properties.

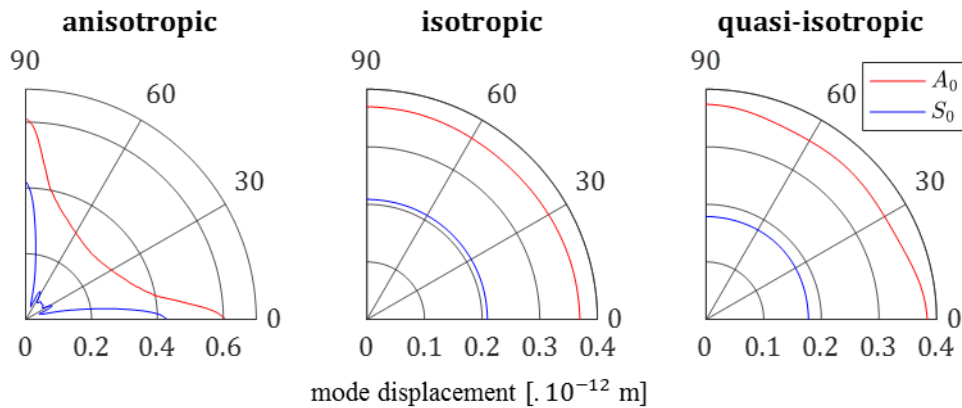


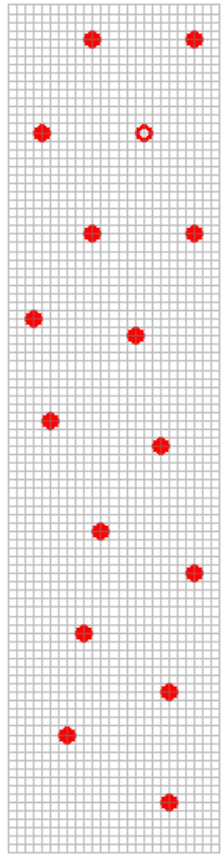
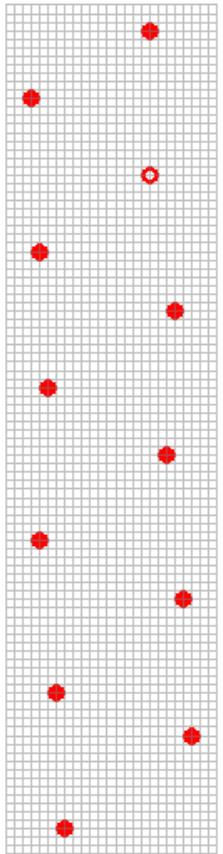
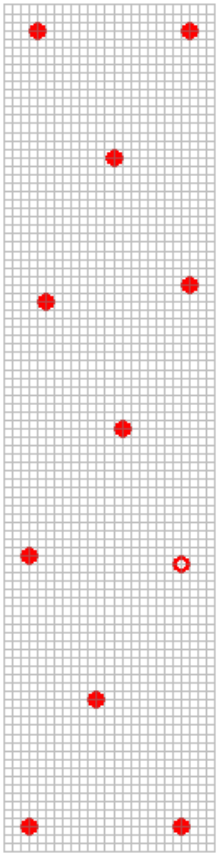
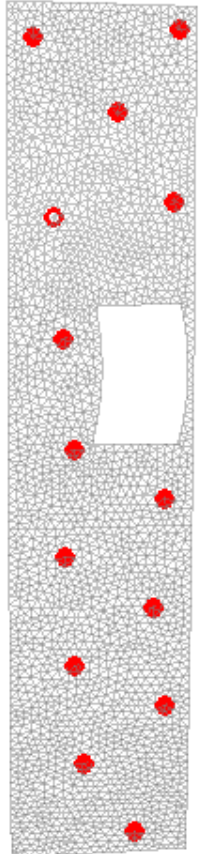
**Figure 15:** Mode attenuation for the three materials used in the tested cases of  $A_0$  (red) and  $S_0$  (blue) with varying orientation at  $f_0 = 100 \text{ kHz}$  and a distance of  $150 \text{ mm}$  from the disk part of the dual PZT used as actuator.

## 400 4.2 Results

401 Table 4 sums up the results obtained for the dual PZT network implementation on the four different  
 402 structures described in the previous paragraph. For each structure, outputs, from each step, are displayed.

403

404 **Table 4:** Application of the process on four different structures

		structure #1	structure #2	structure #3	structure #4
Geometry		Plate	Plate	Plate	Fan Cowl
Material		$[0^\circ/90^\circ]_{16}$	isotropic	$[0^\circ/90^\circ/45^\circ/-45^\circ]_{16}$	$[0^\circ/90^\circ]_{16}$
STEP 1 OUTPUT	$\varnothing_{PZT-disk}$ [mm]	5.5	5.5	5.5	5.5
	$\varnothing_{PZT-ring}^{inner}$ [mm]	7.5	7.5	7.5	7.5
	$\varnothing_{PZT-ring}^{outer}$ [mm]	27.5	27.5	27.5	27.5
	$f_0$ [kHz]	12 ... 134	12 ... 134	13 ... 138	14 ... 134
STEP 2 OUTPUT	$r_{min}$ [mm]	230	150	150	230
	$r_{max}$ [mm]	270	350	360	270
	$\theta_{forbidden}$ $[[\pi/2]^\circ]$	17,73	-	-	17,73
	$f_0$ [kHz]	50 ... 140	50 ... 140	50 ... 140	50 ... 140
STEP 3 OUTPUT	PZT network				
	Number of PZT	16	12	11	14

### 405 4.3 Observations

406 For all structures, same dual PZT dimensions are advised as output of step 1 (see table 4). Actually,  
407 variations of mechanical properties of the material influence more the usable range of frequencies than  
408 the dimensions of the dual PZT. Dual PZT dimensions would be more affected by changing damage  
409 sizes (downsized as the damage size is lowered and vice-versa). For the chosen composite materials,  
410 there is very little variation of the mechanical properties, hence the range of excitation frequencies  
411 obtained with the dispersion curves do not change a lot. The frequency range would be more affected  
412 by a change in the thickness of the material: for a given material if the thickness is divided by  $n$ , the  
413 range of frequencies obtained as output of step 1 would be divided by  $n$ .

414 Comparing results obtained for structure #1 and #2 from table 4 shows the influence of the anisotropy  
415 of the structure on the PZT network. For the isotropic material, there is no amplitude variations of modes  
416 with orientation (see figure 15), and a greater distance between transducers  $r_{max}$  can be achieved with  
417 respect to the superposition and amplitude ratio criteria. This greater distance and the fact that there is  
418 no orientation constrains for structure #2 leads to a smaller PZT network of only 12 dual PZTs, compared  
419 to the 16 obtained on the anisotropic case of structure #1. The minimum distance ( $r_{min} = 150$  mm) of  
420 structure #2 is imposed by the superposition criteria in opposition to #1 where minimum distance  
421 ( $r_{min} = 230$  mm) is imposed by the amplitude ratio criteria.

422 Structure #2 and #3 show very little difference since mode attenuation with orientation for those two  
423 materials is very similar, and in both cases,  $S_0$  and  $A_0$  modes amplitude is constant with orientation  
424 contrary to the anisotropic material (see figure 15).  $S_0$  mode amplitude in the isotropic case is greater  
425 than in the quasi-isotropic case leading to a smaller maximum distance between transducers ( $r_{max} =$   
426 350 mm for structure #2 and  $r_{max} = 360$  mm for structure #3).

427 Comparison of results obtained for structure #1 and #4 from table 4 shows the ability of the algorithm  
428 to be applied on 3D meshes and to provide a PZT network that respects the placement constraints. The  
429 introduction of a cavity in the structure is not really taken into account by the algorithm. It is somehow  
430 considered since no PZT node can be placed in the hole (it does not contain any node), the supplementary

431 constraint on boundary conditions is applied to hole edges, and the computing of distances between  
432 nodes takes the hole into account.

## 433 5. Discussion

434 The proposed method opens several discussion points:

- 435 - The sizing method described in the first step of the process is theoretical. Experimental  
436 measurements often give exploitable results even if the PZT dimensions do not respect the  
437 Lamb wave constraints. However, this theoretical approach is the first attempt to justify the  
438 dual PZT electrodes sizes, and those dimensions are consistent with physical properties of the  
439 structure and lamb wave propagation. There is not only one good sizing, but this method gives  
440 landmarks for the choice of the dual PZT, which is hardly discussed in other studies. The range  
441 of frequencies chosen does not take into account the continuous mode conversion well  
442 described in [9, Pt. IV]. However, by targeting a minimal damage size  $\varnothing_d > 7$  mm (maximum  
443 width of roving in twill fabric composites), wavelengths of both modes obtained on the selected  
444 range of frequencies are larger than the eventual roving thus limiting continuous mode  
445 conversion due to coupling elements. This phenomenon could be responsible for  $A_0$  mode  
446 measurements arriving before the main wave packet in experimental conditions.
- 447 - The thresholds for the superposition criteria and the amplitude ratio criteria may appear  
448 arbitrary but they have been empirically verified. They could be softened if the aim is to place  
449 fewer transducers on the structure or hardened if the aim is to obtain the best mode  
450 decomposition results. This article presents here a concept methodology and some parameters  
451 can be flexible.
- 452 - The large structure presented in this article is not very complex compared to other SHM  
453 applications (only one hole, no stiffener) and the proposed optimization solver would not be  
454 very robust for very complex structures. Still, the local FEM approach could be improved by  
455 integrating stiffeners, holes, and/or complex local geometries preventing the simulation from  
456 modeling the full-scale model at once.

- 457 - Hypotheses done on the local FEM are not very strong and allow to have a good appreciation  
458 of the limiting criteria for the current BF-SHM methods. Even if the model has been calibrated  
459 properly to fit the real material, future works on composite structure will allow the validation  
460 of the obtained optimal parameters meeting the targeted expectations.
- 461 - Results obtained for different structures in part 4 show that a quasi-isotropic structure behaves  
462 quite similarly to an isotropic structure concerning mode attenuation with orientation. This  
463 observation shows that for such a poorly anisotropic structure, the orientation between  
464 transducers has no influence on the designed PZT network, and larger distances can be  
465 considered since the amplitude ratio between  $A_0$  and  $S_0$  modes is nearly constant in all  
466 directions. In the case of the highly anisotropic structure, the amplitude of both modes highly  
467 depends on the propagation orientation, and it has a great impact on the distance and orientation  
468 between transducers.

## 469 6. Conclusion

470 This article presents a process to design a PZT network on a large structure for BF-SHM methods  
471 based on the tracking of mode variations in a composite structure. This work falls within the framework  
472 of research which tries to bridge the gap between laboratory research and industrial deployment of SHM  
473 processes [49]. Indeed, the method proposed in this work tackles one of the problems that hinders the  
474 deployment of a promising dual PZT BF-SHM method, which is how to choose optimally the PZT  
475 elements in terms of size, number and placements.

476 The first contribution of this work, is to propose a generic solution to the choice of dimensions of the  
477 dual PZT (used to decompose  $A_0$  and  $S_0$  mode contributions in the response signal) based on the  
478 dispersion curves and the damage size to detect. This also brings out the range of excitation frequencies  
479 that favor an interaction with the eventual damage.

480 The second contribution resides in the precise and careful exploitation of Lamb wave mode propagation  
481 simulated in a local FEM. Particularly, two criteria are proposed (mode superposition ratio and mode  
482 amplitude ratio) in order to define the best actuator-sensor placement (optimal distance and orientation)

483 and optimal excitation frequencies in a context where both  $A_0$  and  $S_0$  modes have to propagate in the  
484 structure and be measured by the PZT sensor. This local model gives the relevant parameters for the last  
485 key point of this article, which is a simple PZT network optimization solver. This solver guarantees that  
486 dual PZT are optimally placed on the monitored structure, and together with the local FEM avoid the  
487 need for a large-scale FEM simulation.

488 This article does not give an absolute method for a PZT network design but proposes a generic process:  
489 given the material and geometry of a structure, dual PZT size, placement and excitation frequencies are  
490 proposed in order to optimize the implementation of BF-SHM method on the structure to monitor. The  
491 authors have chosen to apply it on four different structures. This emphasizes the need for a local FEM  
492 for highly anisotropic structures to understand the Lamb wave propagation in such materials before  
493 being confronted with unexplainable results in real experimentation.

## 494 References

- 495 [1] K. Worden, C. R. Farrar, G. Manson, and G. Park, "The fundamental axioms of structural health  
496 monitoring," *Proc. R. Soc. Math. Phys. Eng. Sci.*, vol. 463, no. 2082, pp. 1639–1664, Jun. 2007.
- 497 [2] J. E. Michaels and T. E. Michaels, "Detection of structural damage from the local temporal  
498 coherence of diffuse ultrasonic signals," *IEEE Trans. Ultrason. Ferroelectr. Freq. Control*, vol. 52,  
499 no. 10, pp. 1769–1782, Oct. 2005.
- 500 [3] S. Roy, K. Lonkar, V. Janapati, and F.-K. Chang, "A novel physics-based temperature  
501 compensation model for structural health monitoring using ultrasonic guided waves," *Struct. Health  
502 Monit.*, vol. 13, no. 3, pp. 321–342, 2014.
- 503 [4] Y. Wang, L. Gao, S. Yuan, L. Qiu, and X. Qing, "An adaptive filter-based temperature  
504 compensation technique for structural health monitoring," *J. Intell. Mater. Syst. Struct.*, vol. 25, no.  
505 17, pp. 2187–2198, Nov. 2014.
- 506 [5] Y. Wang, L. Qiu, L. Gao, S. Yuan, and X. Qing, "A new temperature compensation method for  
507 guided wave-based structural health monitoring," 2013, p. 86950H.
- 508 [6] G. Konstantinidis, B. W. Drinkwater, and P. D. Wilcox, "The temperature stability of guided wave  
509 structural health monitoring systems," *Smart Mater. Struct.*, vol. 15, no. 4, pp. 967–976, Aug. 2006.
- 510 [7] Y. Lu and J. E. Michaels, "A methodology for structural health monitoring with diffuse ultrasonic  
511 waves in the presence of temperature variations," *Ultrasonics*, vol. 43, no. 9, pp. 717–731, Oct.  
512 2005.
- 513 [8] Z. Su and L. Ye, *Identification of damage using Lamb waves: from fundamentals to applications*.  
514 Berlin: Springer-Verlag, 2009.
- 515 [9] R. Lammering, U. Gabbert, M. Sinapius, T. Schuster, and P. Wierach, Eds., *Lamb-Wave Based  
516 Structural Health Monitoring in Polymer Composites*. Cham: Springer International Publishing,  
517 2018.
- 518 [10] C. M. Yeum, H. Sohn, and J. B. Ihn, "Delamination detection in a composite plate using a dual  
519 piezoelectric transducer network," 2011, p. 798406.

- 520 [11]R. Gangadharan, C. R. L. Murthy, S. Gopalakrishnan, and M. R. Bhat, “Time reversal health  
521 monitoring of composite plates using Lamb waves,” *Int. J. Aerosp. Innov.*, vol. 3, no. 3, pp. 131–  
522 142, 2011.
- 523 [12]L. Huang, L. Zeng, and J. Lin, “Baseline-free damage detection in composite plates based on the  
524 reciprocity principle,” *Smart Mater. Struct.*, vol. 27, no. 1, p. 015026, Jan. 2018.
- 525 [13]V. Giurgiutiu, *Structural health monitoring with piezoelectric wafer active sensors*. Amsterdam:  
526 Academic Press/Elsevier, 2008.
- 527 [14]H. Sohn, H. J. Lim, C. M. Yeum, and J.-B. Ihn, *Reference free inconsistency detection system*.  
528 Google Patents, 2015.
- 529 [15]Y.-K. An and H. Sohn, “Instantaneous crack detection under varying temperature and static loading  
530 conditions,” *Struct. Control Health Monit.*, vol. 17, no. 7, pp. 730–741, Nov. 2010.
- 531 [16]C. M. Yeum, H. Sohn, J. B. Ihn, and H. J. Lim, “Instantaneous delamination detection in a composite  
532 plate using a dual piezoelectric transducer network,” *Compos. Struct.*, vol. 94, no. 12, pp. 3490–  
533 3499, Dec. 2012.
- 534 [17]C. M. Yeum, H. Sohn, H. J. Lim, and J. B. Ihn, “Reference-free delamination detection using Lamb  
535 waves” *Struct. Control Health Monit.*, p. n/a-n/a, Aug. 2013.
- 536 [18]C. M. Yeum, H. Sohn, and J. B. Ihn, “Lamb wave mode decomposition using concentric ring and  
537 circular piezoelectric transducers,” *Wave Motion*, vol. 48, no. 4, pp. 358–370, Jun. 2011.
- 538 [19]H. Sohn and S. B. Kim, “Development of dual PZT transducers for reference-free crack detection  
539 in thin plate structures,” *IEEE Trans. Ultrason. Ferroelectr. Freq. Control*, vol. 57, no. 1, pp. 229–  
540 240, Jan. 2010.
- 541 [20]H. J. Lim, H. Sohn, C. M. Yeum, and J. M. Kim, “Reference-free damage detection, localization,  
542 and quantification in composites,” *J. Acoust. Soc. Am.*, vol. 133, no. 6, pp. 3838–3845, Jun. 2013.
- 543 [21]S. R. Anton, A. Butland, M. Carrión, M. Buechler, and G. Park, “Instantaneous Structural Damage  
544 Identification Using Piezoelectric-Based Lamb Wave Propagation,” *Proc. IMAC-XXV Febr.*, pp.  
545 19–22, 2007.
- 546 [22]S. R. Anton, D. J. Inman, and G. Park, “Reference-Free Damage Detection Using Instantaneous  
547 Baseline Measurements,” *AIAA J.*, vol. 47, no. 8, pp. 1952–1964, Aug. 2009.
- 548 [23]B. Alem, A. Abedian, and K. Nasrollahi-Nasab, “Reference-Free Damage Identification in Plate-  
549 Like Structures Using Lamb-Wave Propagation with Embedded Piezoelectric Sensors,” *J. Aerosp.*  
550 *Eng.*, p. 04016062, Jul. 2016.
- 551 [24]A. Bagheri, K. Li, and P. Rizzo, “Reference-free damage detection by means of wavelet transform  
552 and empirical mode decomposition applied to Lamb waves,” *J. Intell. Mater. Syst. Struct.*, vol. 24,  
553 no. 2, pp. 194–208, Jan. 2013.
- 554 [25]H. Sohn, H. Woo Park, K. Law, and C. R. Farrar, “Combination of a Time Reversal Process and a  
555 Consecutive Outlier Analysis for Baseline-free Damage Diagnosis,” *J. Intell. Mater. Syst. Struct.*,  
556 Dec. 2006.
- 557 [26]Sohn, “Damage Detection in Composite Plates by Using an Enhanced Time Reversal Method.”  
558 2007.
- 559 [27]H. W. Park, H. Sohn, K. H. Law, and C. R. Farrar, “Time reversal active sensing for health  
560 monitoring of a composite plate,” *J. Sound Vib.*, vol. 302, no. 1–2, pp. 50–66, Apr. 2007.
- 561 [28]Z. Liu, X. Zhong, T. Dong, C. He, and B. Wu, “Delamination detection in composite plates by  
562 synthesizing time-reversed Lamb waves and a modified damage imaging algorithm based on  
563 RAPID,” *Struct. Control Health Monit.*, p. n/a-n/a, Jan. 2016.
- 564 [29]H. W. Park, S. B. Kim, and H. Sohn, “Understanding a time reversal process in Lamb wave  
565 propagation,” *Wave Motion*, vol. 46, no. 7, pp. 451–467, Nov. 2009.
- 566 [30]S. B. Kim and H. Sohn, “Instantaneous crack detection using dual PZT transducers,” 2008, p.  
567 693509.
- 568 [31]K. Worden and A. P. Burrows, “Optimal sensor placement for fault detection,” *Eng. Struct.*, vol.  
569 23, no. 8, pp. 885–901, Aug. 2001.
- 570 [32]K. Dogancay and H. Hmam, “On optimal sensor placement for time-difference-of-arrival  
571 localization utilizing uncertainty minimization,” in *Signal Processing Conference, 2009 17th*  
572 *European*, 2009, pp. 1136–1140.
- 573 [33]H. Gao and J. L. Rose, “Ultrasonic Sensor Placement Optimization in Structural Health Monitoring  
574 Using Evolutionary Strategy,” *AIP Conf. Proc.*, vol. 820, no. 1, pp. 1687–1693, Mar. 2006.

- 575 [34]Eric B. Flynn and Michael D. Todd, "Optimal Placement of Piezoelectric Actuators and Sensors for  
576 Detecting Damage in Plate Structures," *J. Intell. Mater. Syst. Struct.*, vol. 21, no. 3, pp. 265–274,  
577 Feb. 2010.
- 578 [35]E. B. Flynn and M. D. Todd, "A Bayesian approach to optimal sensor placement for structural health  
579 monitoring with application to active sensing," *Mech. Syst. Signal Process.*, vol. 24, no. 4, pp. 891–  
580 903, May 2010.
- 581 [36]C. Fendzi, J. Morel, M. Rébillat, M. Guskov, N. Mechbal, and G. Coffignal, "Optimal Sensors  
582 Placement to Enhance Damage Detection in Composite Plates," in *7th European Workshop on*  
583 *Structural Health Monitoring*, 2014, pp. 1–8.
- 584 [37]M. Thiene, Z. S. Khodaei, and M. H. Aliabadi, "Optimal sensor placement for maximum area  
585 coverage (MAC) for damage localization in composite structures," *Smart Mater. Struct.*, vol. 25,  
586 no. 9, p. 095037, Sep. 2016.
- 587 [38]M. S. Salmanpour, Z. Sharif Khodaei, and M. H. Aliabadi, "Transducer placement optimisation  
588 scheme for a delay and sum damage detection algorithm," *Struct. Control Health Monit.*, vol. 24,  
589 no. 4, p. n/a-n/a, Apr. 2017.
- 590 [39]H. Lamb, "On waves in elastic plates," 1917.
- 591 [40]A. Marzani and P. Bocchini, "www.guiguw.com," *GUIGUW - Guided Waves made easy*. [Online].  
592 Available: <http://www.guiguw.com/>. [Accessed: 08-Jun-2018].
- 593 [41]J. L. Rose, *Ultrasonic Waves in Solid Media*. Cambridge University Press, 2004.
- 594 [42]A. Raghavan and C. E. S. Cesnik, "Finite-dimensional piezoelectric transducer modeling for guided  
595 wave based structural health monitoring," *Smart Mater. Struct.*, vol. 14, no. 6, pp. 1448–1461, Dec.  
596 2005.
- 597 [43]E. Balmès, J. Bianchi, and J. Leclere, "Structural Dynamics Toolbox 6.2 (for use with MATLAB),  
598 SDTools, Paris, France.," 2009. [Online]. Available: <http://www.sdtools.com/>. [Accessed: 12-Dec-  
599 2017].
- 600 [44]M. Gresil and V. Giurgiutiu, "Prediction of attenuated guided waves propagation in carbon fiber  
601 composites using Rayleigh damping model," *J. Intell. Mater. Syst. Struct.*, vol. 26, no. 16, pp. 2151–  
602 2169, Nov. 2015.
- 603 [45]E. Balmès, M. Guskov, and J.-P. Bianchi, "Validation and verification of FE models of piezo based  
604 SHM systems," in *ISMA International Conference on Noise and Vibration Engineering*, Leuven,  
605 Belgium, 2016, p. ID 807.
- 606 [46]C. Fendzi, M. Rébillat, N. Mechbal, M. Guskov, and G. Coffignal, "A data-driven temperature  
607 compensation approach for Structural Health Monitoring using Lamb waves," *Struct. Health Monit.*  
608 *Int. J.*, vol. 15, no. 5, pp. 525–540, Sep. 2016.
- 609 [47]Z. Su and L. Ye, "Selective generation of Lamb wave modes and their propagation characteristics  
610 in defective composite laminates," *Proc. Inst. Mech. Eng. Part J. Mater. Des. Appl.*, vol. 218, no.  
611 2, pp. 95–110, Apr. 2004.
- 612 [48]Y.-H. Kim, D.-H. Kim, J.-H. Han, and C.-G. Kim, "Damage assessment in layered composites using  
613 spectral analysis and Lamb wave," *Compos. Part B Eng.*, vol. 38, no. 7–8, pp. 800–809, Oct. 2007.
- 614 [49]P. Cawley, "Structural health monitoring: Closing the gap between research and industrial  
615 deployment," *Struct. Health Monit. Int. J.*, p. 147592171775004, Jan. 2018.
- 616